



Solvothermal synthesis of novel hierarchical $\text{Bi}_4\text{O}_5\text{I}_2$ nanoflakes with highly visible light photocatalytic performance for the degradation of 4-*tert*-butylphenol

Xin Xiao ^{a,*}, Chunlan Xing ^a, Guangping He ^a, Xiaoxi Zuo ^a, Junmin Nan ^{a,b,*}, Lishi Wang ^b

^a School of Chemistry and Environment, South China Normal University; Key Laboratory of the Energy Conversion and Energy Storage Materials of Guangzhou, Guangzhou 510006, PR China

^b Key Laboratory of Fuel Cell Technology of Guangdong Province; School of Chemistry and Chemical Engineering, South China University of Technology, Guangzhou 510640, PR China

ARTICLE INFO

Article history:

Received 1 August 2013

Received in revised form 23 October 2013

Accepted 27 October 2013

Available online 2 November 2013

Keywords:

$\text{Bi}_4\text{O}_5\text{I}_2$ nanoflakes

Solvothermal synthesis

Visible light photocatalysis

4-*Tert*-butylphenol

Photocatalytic mechanism

ABSTRACT

A facile solvothermal route is successfully developed to synthesize $\text{Bi}_4\text{O}_5\text{I}_2$, a novel I-poor bismuth oxyiodide, with hierarchical nanoflake structure. The composition, structure, morphology, formation mechanism, photoabsorption, energy band, and photocatalytic properties of this material are systematically investigated. The results reveal that highly pure $\text{Bi}_4\text{O}_5\text{I}_2$ can be easily obtained by reacting Bi^{3+} , I^- , and OH^- at pH values of 6 to 10 under solvothermal conditions, and the formation of such hierarchical structure can be explained by a dissolution–recrystallization mechanism. The as-synthesized $\text{Bi}_4\text{O}_5\text{I}_2$ nanoflakes show a favorable energy band structure (bandgap energy 2.17 eV, conduction band edge potential is more negative than the reduction potential of superoxide radicals), a high specific surface area ($38.6 \text{ m}^2 \text{ g}^{-1}$), and a hierarchical micro/nano structures. Thus, they exhibit superior photocatalytic and mineralization efficiency for the degradation of 4-*tert*-butylphenol (PTBP, a representative alkylphenol) under visible light irradiation, with a reaction rate is 6.8 and 57 times faster than that of BiOI microspheres and N-doped TiO_2 , respectively. The photogenerated reactive species and degradation intermediates are identified, and possible photocatalytic mechanism is proposed. What's more, the as-synthesized $\text{Bi}_4\text{O}_5\text{I}_2$ nanoflakes remain stable during the photocatalytic reaction and can be used repeatedly, revealing their promising applications in the treatment of organic wastewaters.

© 2013 Elsevier B.V. All rights reserved.

1. Introduction

Environmental pollution and the energy crisis are two major problems in human society that seriously threaten the existence of terrestrial lives [1]. In the past two decades, numerous investigations have focused on semiconductor-based photocatalysts because they may be widely applied for solar energy conversion and environmental purification [2,3]. To date, many semiconductors have been extensively studied as photocatalysts for degrading pollutants or splitting water [4,5]. However, wide-bandgap semiconductors, such as TiO_2 , ZnO , and SnO_2 , are only able to absorb <5% of the solar radiation that reaches the earth's surface, while narrow-bandgap semiconductors, such as Fe_2O_3 , CuO , and CdS , usually exhibit poor photocatalytic performance due to their high carrier recombination rate, low electronic conduction, low oxidation, or poor photo-stability, which greatly limits their practical applications [6]. Therefore, the development of novel, highly

efficient, persistently stable, and visible light driven photocatalysts remains a major challenge.

Recently, as a new family of promising photocatalysts, the bismuth oxyhalides (BiOX , $X = \text{Cl}$ [7], Br [8], and I [9]), have demonstrated remarkable photocatalytic activities because their uniquely layered structure features an internal static electric field perpendicular to each layer that may induce more effective separation of photogenerated charge carriers [10]. Thereinto, BiOI has the smallest band gap and a strong absorption in the visible light region, thus demonstrating excellent photocatalytic efficiency under sunlight irradiation [11]. Aside from BiOI ($\text{O}: \text{I} = 1:1$), other I-poor bismuth oxyiodides, including $\text{Bi}_4\text{O}_5\text{I}_2$ [12], $\text{Bi}_7\text{O}_9\text{I}_3$ [13], $\alpha\text{-Bi}_5\text{O}_7\text{I}$ [14], and $\beta\text{-Bi}_5\text{O}_7\text{I}$ [15], have also been reported. Since the valence band for bismuth oxyiodides mostly contains $\text{O} 2p$ and $\text{I} 5p$ orbitals, while the conduction band is based the $\text{Bi} 6p$ orbital [16], it can be predicted that the I-poor bismuth oxyiodides have bandgap energies that are higher than BiOI but lower than Bi_2O_3 [17,18]; therefore, these materials may be used as visible light induced photocatalysts. More importantly, the composition and structure of the bismuth oxyiodides strongly influences their optical, electronic, oxidizing ability, and other physicochemical properties, offering an

* Corresponding author. Tel.: +86 20 39310255; fax: +86 20 39310187.

E-mail address: jmn@scnu.edu.cn (J. Nan).

opportunity to obtain novel photocatalysts that for effective degradation of environmental pollutants with various features. However, the information describing these bismuth oxyiodides' synthesis, characterization, and evaluated properties has remained scarce until recently, especially for $\text{Bi}_4\text{O}_5\text{I}_2$. Recently, Li and coworkers prepared plate-like $\text{Bi}_4\text{O}_5\text{I}_2$ using a precipitation–filtration process followed by hydrothermal treatment and studied its photocatalytic activity for decomposition of methyl orange [19]. To investigate the photocatalytic properties of oxygen-rich bismuth oxyhalides, we synthesized $\text{Bi}_4\text{O}_5\text{I}_2$ using commercial Bi_2O_3 , HNO_3 , and KI under hydrothermal conditions, and preliminary evaluated its photocatalytic activity for the degradation of bisphenol-A [17]. Nevertheless, due to the restricted crystal growth under the routine depositing conditions, synthesizing nanostructured $\text{Bi}_4\text{O}_5\text{I}_2$ via wet chemical processes remains a major challenge. What's more, the formation conditions, optical properties, electronic structure, photocatalytic activity, and visible light induced photocatalytic mechanism for $\text{Bi}_4\text{O}_5\text{I}_2$ also require further investigation.

As a representative alkylphenol, 4-*tert*-butylphenol (PTBP) is an important industrial chemical that is widely used to make phosphate esters, fragrances, oil field chemicals, detergents, and demulsifiers [20]. Owing to its widespread use, a considerable amount of PTBP has been released into aquatic environments, causing its frequent detection in river and seawaters [21], as well as in aquatic animals [22] and human urine [23]. PTBP is now recognized as a serious aquatic pollutant because it persists in the environment and demonstrates acute and chronic toxicities [24], in addition to estrogenic activity [25,26]. Therefore, removing PTBP from aquatic environments is crucial for environmental protection [27]. However, although heterogeneous photocatalysis are potentially advantageous for the degradation of organic contaminants in water, the photocatalytic decomposition of PTBP has hardly been investigated [28]. To the best of our knowledge, the degradation of PTBP over a non-titania photocatalyst utilizing visible light irradiation has not been reported. In this paper, novel hierarchical $\text{Bi}_4\text{O}_5\text{I}_2$ nanoflakes were synthesized using a solvothermal route; their structure, morphology, photoabsorption, band structure, and specific surface properties were characterized. And then, the $\text{Bi}_4\text{O}_5\text{I}_2$ nanoflakes' photocatalytic and mineralization efficiency for PTBP degradation was evaluated under visible light irradiation, the photogenerated reactive species and degradation intermediates were identified, and possible photocatalytic mechanism was proposed.

2. Experimental

2.1. Materials and methods

The PTBP was obtained from Aladdin Reagent Co., Ltd. The Bismuth nitrate pentahydrate ($\text{Bi}(\text{NO}_3)_3 \cdot 5\text{H}_2\text{O}$) and potassium iodide (KI) were purchased from Tianjin Kermel Chemical Reagent Co., Ltd. Ethylene glycol (EG) was bought from Chinasun Specialty Products Co., Ltd. All of the chemicals were analytical grade and used as received.

The $\text{Bi}_4\text{O}_5\text{I}_2$ nanoflakes were synthesized using a solvothermal route. In a typical synthesis, 0.728 g $\text{Bi}(\text{NO}_3)_3 \cdot 5\text{H}_2\text{O}$ and 0.498 g KI were orderly dissolved in 35 mL EG with magnetic stirring at room temperature, and then the pH of the system was adjusted to 9 using 2 mol L^{-1} NaOH . Afterwards, the mixture was poured into a Teflon-lined stainless-steel autoclave (45 mL capacity) and incubated in an oven at 150 °C for 12 h. After completion of the reaction, the precipitates were collected by centrifugation, washed several times with distilled water and ethanol to remove any ionic residue, and finally dried in an oven at 60 °C.

For comparison, a BiOI sample was synthesized using the same process but without adding the NaOH solution. Additionally, an

N-doped TiO_2 (N-TiO₂) sample was prepared by a solvothermal method using ethylenediamine as the nitrogen source, as described by Yang et al. [29] (Fig. S1, Supporting information).

2.2. Crystal structure and theoretical calculation

The crystal structure of $\text{Bi}_4\text{O}_5\text{I}_2$ was modified from that of $\text{Bi}_4\text{O}_5\text{Br}_2$ (ICSD-94498) with replacement of Br by I on the structure, and the details were refined according to previous reports [30]. Subsequently, the crystal structure of $\text{Bi}_4\text{O}_5\text{I}_2$ was used to calculate the theoretical powder diffraction pattern using the Diamond software. The band structure calculations were performed with the Cambridge Serial Total Energy Package (CASTEP) code within Materials Studio that was based on the density functional theory (DFT). Ultrasoft pseudopotentials were used for the geometric optimization to make the computations more tractable and efficient. The exchange and correlation interactions were modeled using the generalized gradient approximation (GGA), together with the Perdew–Burke–Ernzerhof (PBE). A plane-wave cutoff energy of 340 eV was employed. The energies and electronic structures were calculated based on the optimized geometric structures.

2.3. Catalyst characterization

The crystalline structures of the samples were determined using powder X-ray diffraction (XRD) with a Bruker D8 Advance (Bruker AXS, Germany) X-ray diffractometer with $\text{Cu K}\alpha$. The sample's surface composition was analyzed using X-ray photoelectron spectroscopy (XPS, Thermo Scientific ESCALAB 250Xi, USA) equipped with an $\text{Al K}\alpha$ source. And the valence band X-ray photoelectron spectroscopy (VB XPS) of as-prepared samples were acquired with an energy step of 0.100 eV. The morphology and structure were examined using scanning electron microscopy (SEM, JSM-6510, JEOL, Japan) and transmission electron microscopy (TEM, JEM-2100HR, Japan). The iodide content in the sample was determined with an ion chromatograph (IC, Dionex ICS 900, USA) equipped with an anion exchange column and an electrical conductivity detector. The specific surface areas were measured using nitrogen adsorption–desorption isotherms at 77 K according to the Brunauer–Emmett–Teller analysis (BET, ASAP 2020, Micromeritics, USA). A desorption isotherm was used to determine the pore size distribution using the Barrett–Joyner–Halenda (BJH) method. The UV–vis diffuse reflection spectra (DRS) was recorded on a UV–vis spectrophotometer (UV-3010, Hitachi, Japan) by using BaSO_4 as a reference and was converted from reflection to absorbance by the Kubelka–Munk method.

2.4. Photocatalytic activity measurements

The photocatalytic degradation experiments were performed in a photochemical reactor (XPA-VII, Xujiang, China) equipped with a 1000 W Xe lamp combined with a 420 nm cutoff filter as the light source, and the system was cooled with a circulating water bath maintained at room temperature. All photocatalytic reactions were performed using the same initial conditions: 50 mL reaction solution containing PTBP at various initial concentrations (from 20 to 100 mg L^{-1} , typically 60 mg L^{-1}) was mixed with an as-synthesized photocatalyst (varying from 0.5 to 2.5 g L^{-1} , typically 1.0 g L^{-1}) with constant magnetic stirring. Before irradiation, the solution containing the catalyst was stirred for 1 h in the dark to allow the system to reach adsorption equilibrium. During the photocatalytic process, approximately 3 mL of the suspension was taken out at a specified time, and subsequently, the solids were removed from the solution using a 0.45 μm nitrocellulose filter and the filtrate was then

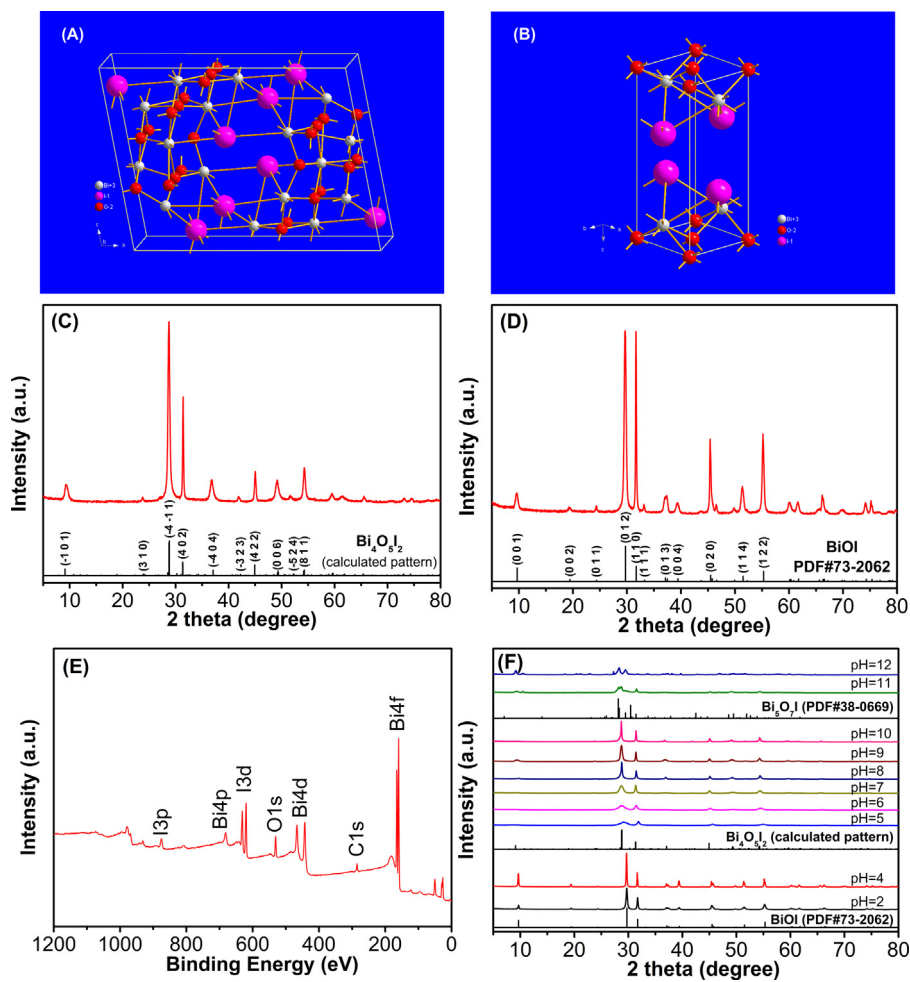


Fig. 1. ((A) and (B)) Schematic representation of the crystal structures of $\text{Bi}_4\text{O}_5\text{I}_2$ and BiOI ; ((C) and (D)) XRD patterns of the as-synthesized $\text{Bi}_4\text{O}_5\text{I}_2$ and BiOI ; (E) XPS spectrum of the as-synthesized $\text{Bi}_4\text{O}_5\text{I}_2$; and (F) XRD patterns of samples prepared over pH 2 to 12.

examined using UV-vis spectroscopy (UV-1800, Shimadzu, Japan, $\lambda = 274 \text{ nm}$) to obtain the PTBP concentrations.

2.5. Analytical methods

The sample solutions were separated with a high-performance liquid chromatography (HPLC, LC-10AT, Shimadzu, Kyoto, Japan) equipped with a UV detector using a C18 reversed phase column ($5 \mu\text{m}$, $4.6 \times 250 \text{ mm}$) at 30°C . The injection volume was $20 \mu\text{L}$, and the mobile phase was composed of methanol/water ($70/30$, v/v) flowing at 1 mL min^{-1} . A coupled liquid chromatography/mass spectrometry (LC/MS, Thermo Finnigan LCQ Deca XP Max, USA) equipped with an electrospray ionization source was utilized to acquire the spectra of PTBP and its oxidation products; negative ionization (NI) and selective ion monitoring (SIM) modes with a dwell time of 200 ms and a scan range of 70–250 Da were used. The intermediates formed during the photocatalytic degradation were further analyzed by gas chromatography-mass spectrometry (GC-MS, DSQ/Trace GC Ultra, Thermo Fisher Scientific, Dreieich, Germany) using a DB 5-MS column ($30 \text{ m} \times 0.25 \text{ mm}$). The sample solutions after photocatalytic reaction were acidified with 1 mol L^{-1} HCl to pH 2–3, extracted three times with an ethyl acetate/n-hexane mixture (2:1, v/v). Then all of the organic layer were collected and concentrated to about 1 mL using a gentle stream of high-purity nitrogen. The column temperature of GC was maintained at 50°C for 2 min, increased to 250°C at $10^\circ\text{C min}^{-1}$, and then held at 250°C for 20 min. The injector and transfer line

temperatures were both 230°C . Helium gas was used as the carrier gas at a flow rate of 1.2 mL min^{-1} . The ion source temperature of MS is 250°C , and electron energy is 70 eV. The total organic carbon (TOC) content was measured with an automatic total organic carbon analyzer (TOC-V, Shimadzu, Japan). Electron paramagnetic resonance (EPR) spectra were recorded at room temperature using JES FA-200 spectrometer (JEOL, Japan) equipped with a 500W Xe lamp and a cut-off filter ($\lambda > 420 \text{ nm}$). And 5,5-dimethyl-1-pyrroline-N-oxide (DMPO) was used as a spin trap.

3. Results and discussion

3.1. Characterization of $\text{Bi}_4\text{O}_5\text{I}_2$

3.1.1. Structure and composition

XRD patterns can provide the crystal and phase information of the as-synthesized samples. Since there was no a standard JCPDS card corresponding to the characteristic peaks of $\text{Bi}_4\text{O}_5\text{I}_2$, the crystal structure of $\text{Bi}_4\text{O}_5\text{I}_2$ was initially built according to the previously reported data [30], as displayed in Fig. 1A. It is clearly shown that the $\text{Bi}_4\text{O}_5\text{I}_2$ is monoclinic phase (space group $P1211$) and is therefore very different from BiOI (tetragonal phase, interleaved with $[\text{Bi}_2\text{O}_2]$ slabs and double iodine atoms slabs, Fig. 1B). Subsequently, the crystal structure of $\text{Bi}_4\text{O}_5\text{I}_2$ was used to calculate the theoretical powder diffraction pattern for comparison with the experimental diffractogram. As depicted in Fig. 1C, all diffraction peaks from the as-synthesized sample (addition

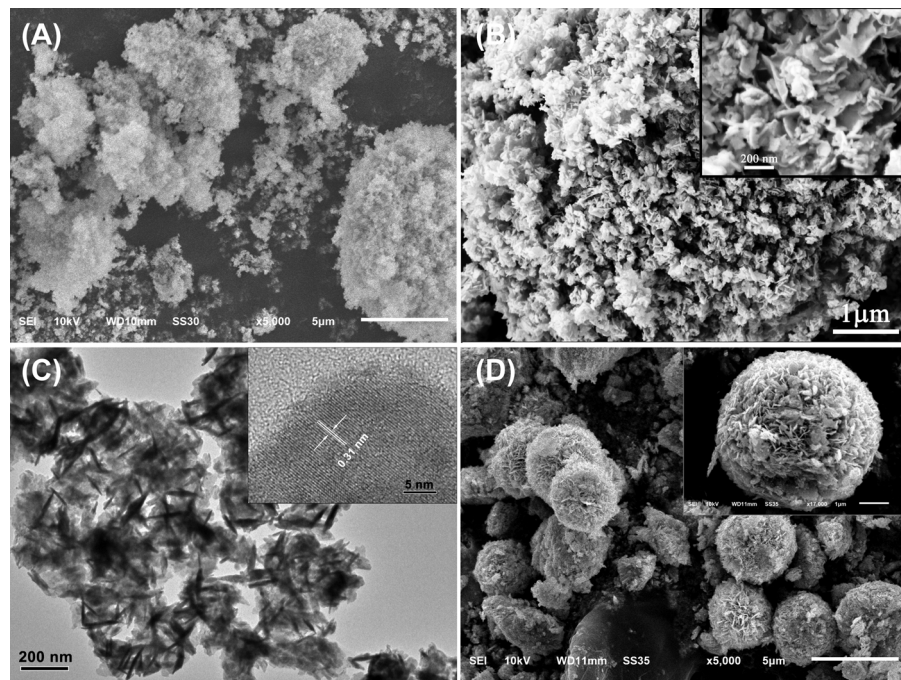


Fig. 2. ((A) and (B)) SEM images of *as*-synthesized $\text{Bi}_4\text{O}_5\text{I}_2$; (C) TEM image of $\text{Bi}_4\text{O}_5\text{I}_2$, the inset contains a high-resolution TEM image of the $\text{Bi}_4\text{O}_5\text{I}_2$ nanoflakes; and (D) SEM image of *as*-synthesized BiOI .

NaOH , pH 9) closely matched the calculated pattern for $\text{Bi}_4\text{O}_5\text{I}_2$. Whereas, diffraction peaks of the contrasting sample (without addition NaOH , pH ~0.5) was clearly indexed as the tetragonal phase of BiOI (JCPDS card No. 73-2062, Fig. 1D), agreeing with reported data [11]. The results suggest that alkali plays a key role during the formation of bismuth oxyiodides with different oxygen–iodine ratios.

The XPS technique supplies semi-quantitative estimation of the elements and chemical state data present on sample surfaces. The XPS result (Fig. 1E) reveals that the *as*-synthesized sample is an I-poor bismuth oxyiodide with a 3.85:5.19:2 of $\text{Bi}/\text{O}/\text{I}$ based on the areas of the Bi , O , and I peaks within experimental error; this ratio is close to the ideal ratio for $\text{Bi}_4\text{O}_5\text{I}_2$, and the excess oxygen atoms may be attributed to chemisorbed H_2O or OH^- on the sample's surface. In addition, the *as*-synthesized sample was completely dissolved in sulfuric acid solution, and then the concentration of I^- was determined by an ion chromatography (IC). The result shows that the solution's iodine content was 4.59 mg L^{-1} , which closely matching the preparation concentration (5 mg L^{-1}) (Fig. S2, Supporting information). Moreover, thermogravimetric method was applied to further verify the sample's iodine content. The *as*-synthesized sample was vacuum-dried and calcined in air at 850°C for 3 h to convert it completely to Bi_2O_3 . Then the weight loss of the sample was calculated to be 20.44%, which is very similar to the theoretical value (20.33%). Therefore, the *as*-synthesized sample was fully characterized as $\text{Bi}_4\text{O}_5\text{I}_2$.

To investigate the role of OH^- during the synthesis, eight other samples were prepared using the same process except the pH was varied to 2, 4, 5, 6, 7, 8, 10, 11, and 12. As displayed in Fig. 1F, for the samples synthesized at pH < 5, the diffraction data obtained match well with tetragonal BiOI (JCPDS card No. 73-2062). As the pH value was increased to 5, new diffraction peaks appeared, which could be identified as the $\text{Bi}_4\text{O}_5\text{I}_2$, yet impurity peaks could be identified as BiOI , indicating that the sample is mixed of BiOI and $\text{Bi}_4\text{O}_5\text{I}_2$. When the pH value was increased from 6 to 10, the obtained products could be identified as the $\text{Bi}_4\text{O}_5\text{I}_2$ and no any obvious impurity peak was observed, although the diffraction intensity of samples increased with the increase of pH, implying that the $\text{Bi}_4\text{O}_5\text{I}_2$ could

be obtained over a wide pH range. The product obtained at pH = 12 is identified as the monoclinic phase $\text{Bi}_5\text{O}_7\text{I}$ (JCPDS card no. 38-0669), while the product prepared at pH 11 represents a mixed phase of $\text{Bi}_4\text{O}_5\text{I}_2$ and $\text{Bi}_5\text{O}_7\text{I}$. The result is close to Li's report on the synthesis of BiOI , $\text{Bi}_4\text{O}_5\text{I}_2$, and $\text{Bi}_5\text{O}_7\text{I}$ using hydrothermal treatment [19].

3.1.2. Morphology and possible formation process

The morphology and microstructure of the *as*-synthesized $\text{Bi}_4\text{O}_5\text{I}_2$ and BiOI were characterized. It can be observed from Fig. 2 that the SEM image of $\text{Bi}_4\text{O}_5\text{I}_2$ (Fig. 2A and B) is completely different with that of BiOI (Fig. 2D). The BiOI sample appears three-dimensional (3D) nanosheet-constructed microspheres approximately $3 \mu\text{m}$ in diameter, which agrees with the previous report [11]. However, the *as*-synthesized $\text{Bi}_4\text{O}_5\text{I}_2$ displays a three-dimensional (3D) hierarchical micro/nano structure, which is composed of numerous nanoflakes, these nanoflakes are significantly smaller than that of BiOI nanosheets with less than 15 nm thick and $100\text{--}300 \text{ nm}$ in the other two dimensions (Fig. 2B), and are connected to each other to form micro-sized particles (Fig. 2A). The result can be further confirmed by the TEM observation (Fig. 2C). The result of TEM also means that these micro/nano-architectures are sufficiently stable that cannot be destroyed into disperse nanoflakes after ultrasonic treatment. In addition, the corresponding high-resolution TEM image in the inset of Fig. 2C depicts a clearly resolved crystalline domain with a uniform interplanar spacing of $\sim 0.31 \text{ nm}$, corresponding to the $(-4-11)$ plane of the monoclinic $\text{Bi}_4\text{O}_5\text{I}_2$.

To elucidate the growth process of the $\text{Bi}_4\text{O}_5\text{I}_2$ macro/nano-structures, time-dependent experiments were carried out, and the resulting products were collected at different stages and analyzed with XRD and SEM. As presented in Fig. 3A, the diffraction peaks for the sample obtained before the solvothermal treatment revealed a mixture of $\text{Bi}_4\text{O}_5\text{I}_2$ and BiOI phases and a low degree of crystallinity. The corresponding SEM image (Fig. 3B) suggests that it contains irregular particles about $0.5\text{--}3 \mu\text{m}$ in diameter. However, after the solvothermal reaction, the crystallinity of the samples increased significantly, and pure $\text{Bi}_4\text{O}_5\text{I}_2$ phases were obtained. The corresponding SEM images (Fig. 3C and D, and Fig. 2A and

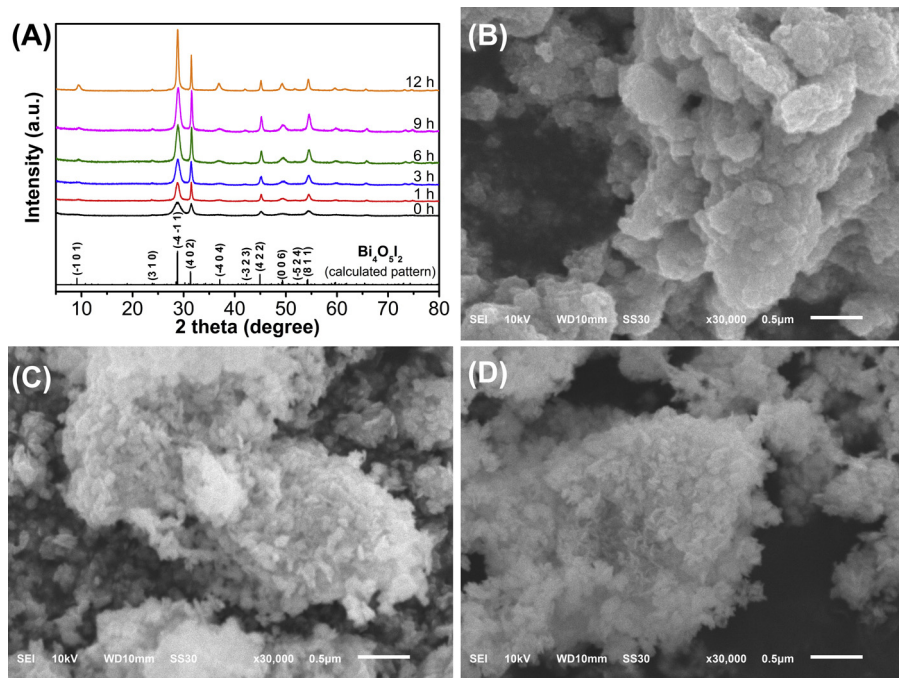


Fig. 3. (A) XRD patterns of samples obtained before (0 h) and after 1, 3, 6, 9, and 12 h of solvothermal reaction; SEM images of the sample obtained (B) before and after solvothermal reaction for (C) 3 h and (D) 6 h.

B) demonstrate that the nanoflakes were generated on the irregular particles' surface gradually. Over prolonged reaction times, the nanoflakes increased rapidly in number while their thickness decreased, which may be ascribed to a dissolution-recrystallization process occurring during the solvothermal reaction, and the micro-sized particles act as the self-sacrificing templates. Eventually, $\text{Bi}_4\text{O}_5\text{I}_2$ with a hierarchical micro/nano structures was obtained.

Based on the above observations, the possible processes for BiOI and $\text{Bi}_4\text{O}_5\text{I}_2$ formation are proposed as follows: in the system without added NaOH ($\text{pH} \sim 0.5$), EG acts as a coordinating agent, preventing the rapid hydrolysis of $\text{Bi}(\text{NO}_3)_3$ [31]. When the reaction system reaches a high temperature, BiOI will be produced by react with Bi^{3+} , I^- , and H_2O (Eq. (1)). These newly formed BiOI nuclei then developed into nanosheets due to the intrinsic crystalline nature of BiOX [32], and tended to aggregate into larger particles to reduce their surface energy [33]. Because fewer surface hydroxyl groups were available and the viscosity was higher in the EG-mediated process, the nanosheets rotated to find a low-energy configuration interface, forming perfectly oriented assemblies [34]. Therefore, BiOI containing 3D microsphere structures was formed. However, when NaOH solution was added to the reaction system, the $\text{Bi}(\text{NO}_3)_3$ hydrolyzed quickly before heating, and BiOI formed immediately. Under the basic reaction conditions, OH^- may gradually replace I^- , forming I-poor bismuth oxyiodides in a similar manner to the previously reported synthesis of $\text{Bi}_5\text{O}_7\text{I}$ using BiOI and NaOH [35]. At suitable pH conditions (from 6 to 10) as well as a high temperature solvothermal process, highly crystalline $\text{Bi}_4\text{O}_5\text{I}_2$ was finally obtained (Eq. (2)). Concurrently, the hierarchical nanoflakes structures were developed according to the dissolution-recrystallization mechanism.



3.1.3. Photoabsorption and energy band structure

The energy band structural features of a semiconductor are considered as a key factor to determine a material's photocatalytic

activity [36]. Fig. 4A shows the UV-vis diffuse reflection spectra (DRS) of the *as*-synthesized samples. The maximal absorbance wavelengths of $\text{Bi}_4\text{O}_5\text{I}_2$ and BiOI are approximately 568 and 680 nm, respectively. Correspondingly, the materials display significantly different colors from yellow to red (inset of Fig. 4A). The band gap energy of these samples may then be evaluated using the following equation (Eq. (3)) [17]:

$$\alpha(h\nu) = A(h\nu - E_g)^{n/2} \quad (3)$$

where α , ν , E_g and A are the absorption coefficient, light frequency, band gap energy, and a constant, respectively, and n depends on the characteristics of the transition in a semiconductor. For BiOX , n is 4 for its indirect transition [37]. Then the band gap energies of the *as*-synthesized samples were estimated using a plot of $(\alpha h\nu)^{1/2}$ vs. photon energy ($h\nu$) (displayed in the inset of Fig. 4A) to be approximately 2.17 and 1.83 eV for $\text{Bi}_4\text{O}_5\text{I}_2$ and BiOI , respectively. The E_g values for $\text{Bi}_4\text{O}_5\text{I}_2$ and BiOI determined in this work are close to those reported in the literatures [17,19].

As an effective photocatalyst, its potential of valence band (E_{VB}) and conduction band (E_{CB}) should be located in an appropriate position so that photogenerated charge carriers can take part in decomposing organic molecules. To determine the valence band (VB) edges of the *as*-synthesized photocatalysts, the total densities of VB states of the samples were measured by VB XPS [38–40]. As shown in Fig. 4B, the VB top of BiOI and $\text{Bi}_4\text{O}_5\text{I}_2$ were determined to be 1.42 and 1.61 eV, respectively, by linearly extrapolating the leading edge at its maximum slope point to the baseline. And the conduction band (CB) bottom potentials of the two semiconductors can be obtained by using the equation of $E_{CB} = E_{VB} - E_g$. Then the comparison of the band structures of $\text{Bi}_4\text{O}_5\text{I}_2$ and BiOI are shown in Fig. 4C, which clearly reveals that $\text{Bi}_4\text{O}_5\text{I}_2$ demonstrates a more positive valence band potential as well as a more negative conduction band potential than that of BiOI , implying it has stronger redox ability. In addition, it is generally believed that the reduction potentials of $\cdot\text{OH}/\text{OH}^-$ and O_2/O_2^- are 2.3 and -0.33 V vs. NHE, respectively [10]. Therefore, neither $\text{Bi}_4\text{O}_5\text{I}_2$ nor BiOI is able to

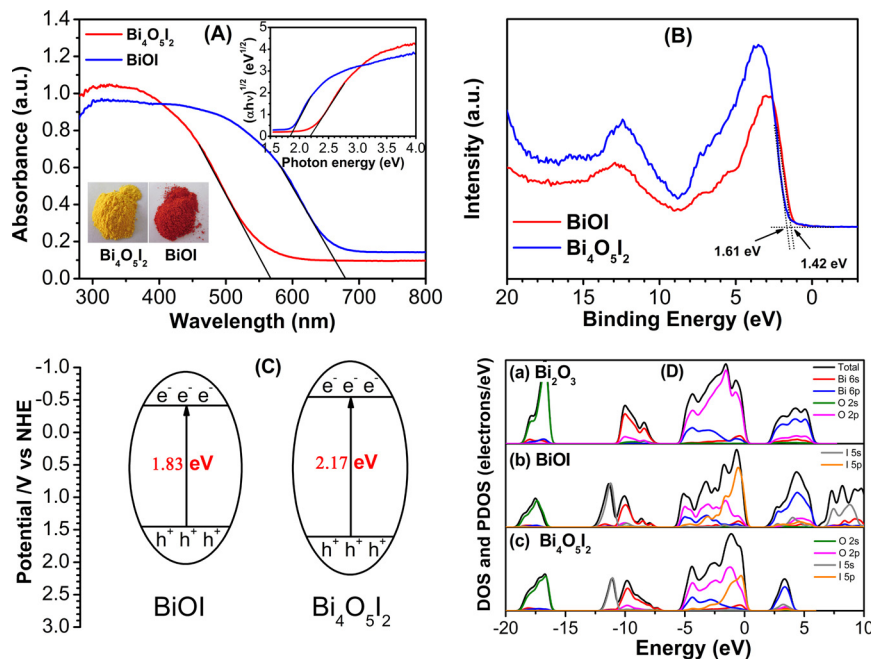


Fig. 4. (A) UV–vis diffuse reflection spectra (DRS) for BiOI and Bi₄O₅I₂, the inset displays plots of $(\alpha h\nu)^{1/2}$ vs. photon energy ($h\nu$); (B) VB XPS spectra of the *as-synthesized* BiOI and Bi₄O₅I₂; (C) Estimated band positions for BiOI and Bi₄O₅I₂; (D) The density of states (DOS) and partial density of states (PDOS) for (a) Bi₂O₃, (b) BiOI, and (c) Bi₄O₅I₂. (For interpretation of the references to color in this figure legend, the reader is referred to the web version of this article.)

oxidize the surface hydroxyl groups or water to generate ·OH, yet it is feasible for Bi₄O₅I₂ to trap molecular oxygen to generate ·O₂[−].

To further understand the effects of the iodide content on the electronic band structure of bismuth oxyiodides, the density of states (DOS) of BiOI and Bi₄O₅I₂ were calculated using density functional theory (DFT) with the generalized gradient approximation (GGA), and the results were compared to the data of Bi₂O₃. As is shown in Fig. 4D, the VB maximum of Bi₂O₃ mainly contributed to the O 2p state, while the Bi 6p state dominated the CB minimum. For BiOI, the Bi 6p state contributed to the CB bottom, while the I 5p state dominated its VB top, reducing its band gap energy relative to Bi₂O₃ [16]. However, in the Bi₄O₅I₂ system, both the O 2p and I 5p states contributed its VB top, while both Bi 6p and I 5s states dominated most of the CB bottom. Consequently, the band gap energy for Bi₄O₅I₂ is larger than for BiOI but smaller than for Bi₂O₃ (the measured band gap energy of β-Bi₂O₃ was approximately 2.4 eV). These results agree with previous experimental results and highlight these materials' different oxidation-reduction abilities during the degradation of pollutants [41,42].

3.1.4. Specific surface area and pore structure

The specific surface area of a semiconductor is considered as another key factor that affects its photocatalytic efficiency. Fig. 5 contains the isotherms for both hierarchical Bi₄O₅I₂ nanoflakes and the 3D BiOI microspheres. Both isotherms are type IV with a H3 hysteresis loop, suggesting that they are mesoporous feature [43]. The BET surface areas of the samples were then calculated using the N₂ isotherms and found to be 38.6 m² g^{−1} for Bi₄O₅I₂ nanoflakes and 18.1 m² g^{−1} for BiOI microspheres, indicating that the specific surface area of the former is more than twice as large as the latter. The corresponding pore size distributions of the *as-synthesized* Bi₄O₅I₂ and BiOI determined with the BJH method revealed that the mesoporous average diameters were 20.5 nm for Bi₄O₅I₂ and 22.6 nm for BiOI and broadly distributed, as illustrated by the inset in Fig. 5. The mesoporous feature with broadly distributed pores may arise from the inter-nanoflake/nanosheet spaces within these two systems.

3.2. Photocatalytic degradation of 4-tert-butylphenol

3.2.1. Evaluation of photocatalytic activity and TOC mineralization

The photocatalytic degradation of PTBP on the *as-synthesized* Bi₄O₅I₂ nanoflakes was evaluated under visible light irradiation and compared to the degradation activity of blank (no photocatalyst), BiOI microspheres, and N-TiO₂, as displayed in Fig. 6A. It is clearly shown that the PTBP was hardly be diminished under visible light irradiation. Under identical irradiation for 90 min, only 9.6% degradation occurred when the N-TiO₂ was used, while the BiOI microspheres achieved a degradation efficiency of 48.0%. However, a 99.8% removal ratio was attained using the Bi₄O₅I₂ nanoflakes, demonstrating that the *as-synthesized* Bi₄O₅I₂ displays excellent activity under visible light for PTBP degradation. The low activity of the N-TiO₂ might be caused by its larger particle size (Fig. S1B,

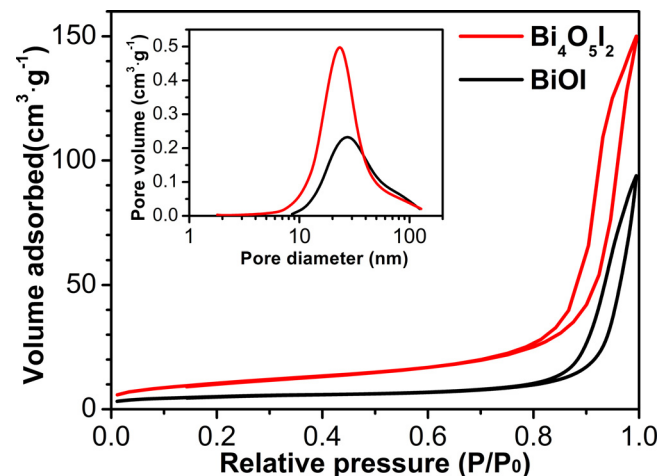


Fig. 5. Nitrogen adsorption–desorption isotherms and the corresponding pore size distribution (inset) for the *as-synthesized* Bi₄O₅I₂ and BiOI.

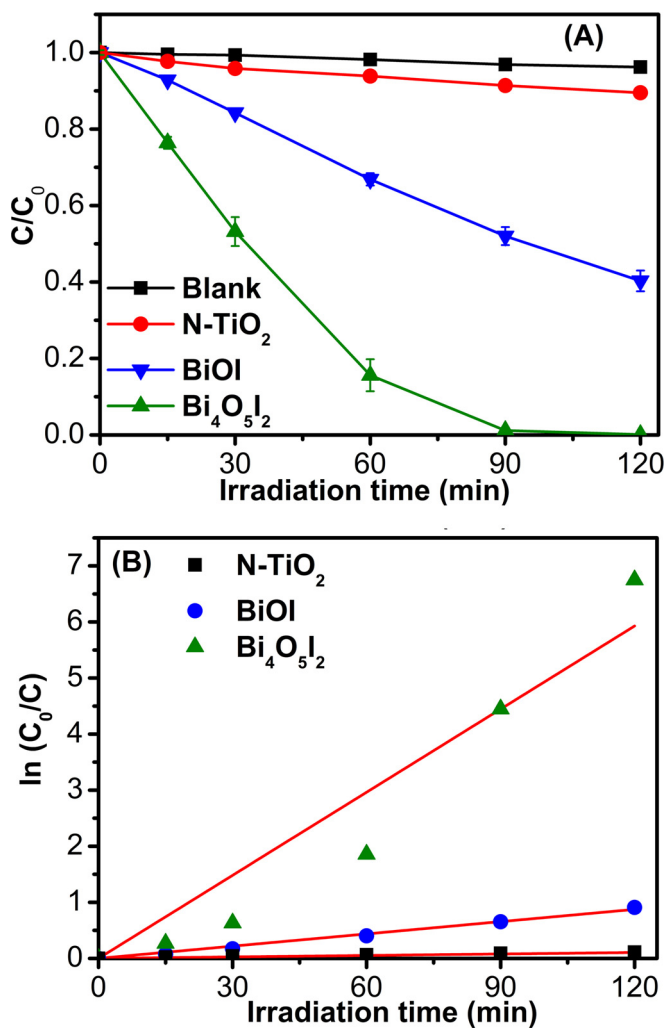


Fig. 6. (A) Photocatalytic degradation kinetics of PTBP with an initial concentration of 60 mg L⁻¹ and 1 g L⁻¹ catalyst on blank (without catalyst), N-TiO₂, BiOI, and Bi₄O₅I₂ under visible light irradiation; (B) Linear plots of ln(C₀/C_t) vs. degradation time.

Supporting information) and relatively poor absorption in the visible light region [29].

The degradation kinetics of PTBP when using synthetic Bi₄O₅I₂ nanoflakes, BiOI microspheres, and N-TiO₂ were investigated by fitting the experimental data to the Langmuir–Hinshelwood model [44]. Because the reactant concentration was low, the following pseudo first-order kinetics equation (Eq. (4)) was used:

$$-\ln\left(\frac{C_t}{C_0}\right) = k_{app}t \quad (4)$$

where C₀ and C_t are the reactant concentrations at t=0 and t, respectively, and k_{app} (min⁻¹) is the apparent reaction rate constant determined by plotting ln(C₀/C_t) vs. the reaction time (t). The results show that the reaction kinetics of all samples can be fitted well by the pseudo first-order rate model with good correlation coefficients, as indicated by Fig. 6B. The calculated k_{app} values for Bi₄O₅I₂, BiOI, and N-TiO₂ were 0.0494, 0.00728, and 0.000874 min⁻¹, respectively. Namely, the apparent reaction rate constant for the as-synthesized Bi₄O₅I₂ nanoflakes was 6.8 and 57 times higher than the rate constants of the BiOI microspheres and N-TiO₂, respectively.

Several factors may account for the high photocatalytic activity of the as-synthesized hierarchical Bi₄O₅I₂ nanoflakes. First, Bi₄O₅I₂ has a favorable band structure that ensures it efficiently utilizes

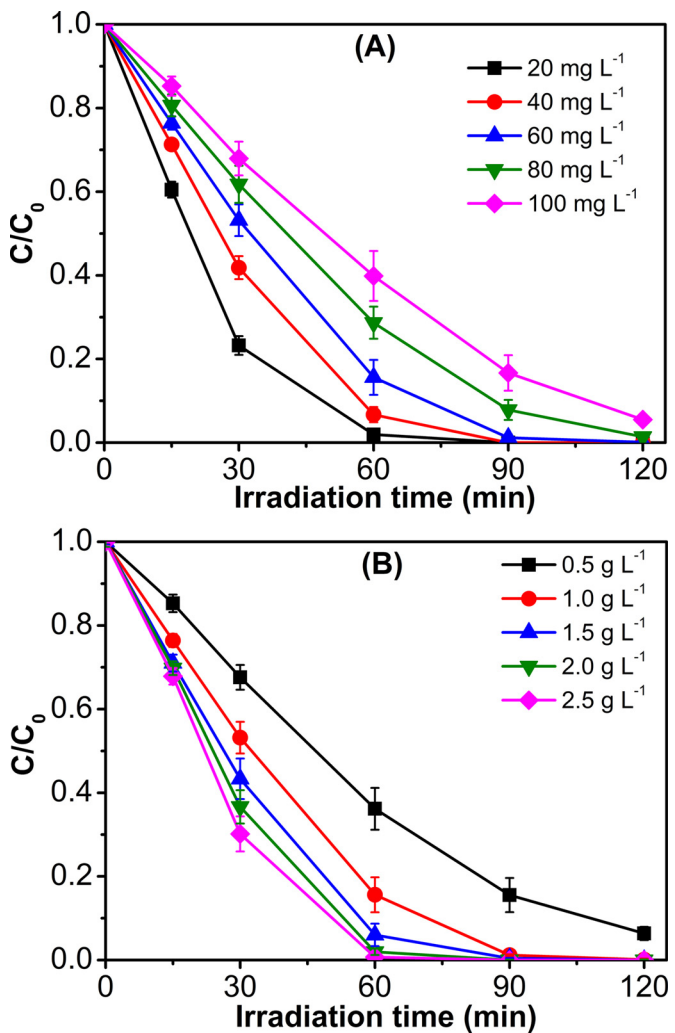


Fig. 7. Effects of (A) the initial concentration of PTBP and (B) the catalyst dose on the photocatalytic performance of the Bi₄O₅I₂ nanoflakes. Experimental conditions: catalyst dose is 1 g L⁻¹ for PTBP concentration experiments, while C₀ = 60 mg L⁻¹ for the experiments using a varied catalyst dose.

the visible light, as well as has strong redox ability during photocatalytic degradation. Second, it is generally accepted that the catalytic process depends mainly on the adsorption of reactant molecules to the catalyst surface [45]. The as-synthesized Bi₄O₅I₂ nanoflakes' higher specific surface area with mesoporous feature allows more efficient transport for the reactant molecules to access its active sites, hence enhancing the photocatalytic efficiency [46]. Thirdly, high photocatalytic efficiency is related to the hierarchical micro/nano structures of the as-synthesized Bi₄O₅I₂. Such 3D interconnected channels formed by Bi₄O₅I₂ nanoflakes provided high surface-to-volume ratios, and generated efficient transport pathways for the reactants and oxidation products during photocatalytic reactions [47].

Different initial concentrations of PTBP solutions (ranging from 20 to 100 mg L⁻¹) and varied Bi₄O₅I₂ doses (from 0.5 to 2.5 g L⁻¹) were used to study the effects of the operating conditions on the photocatalytic system. It is observed from Fig. 7A that lower PTBP concentrations degrade more efficiently. This may be associated with that as the initial concentration of PTBP increases, additional organic molecules are able to absorb on the photocatalyst's surface, reducing the photogeneration of the reactive oxygen species due to overloading of the active sites. In addition, increasing the PTBP concentration leads to an increase in the amount of incident

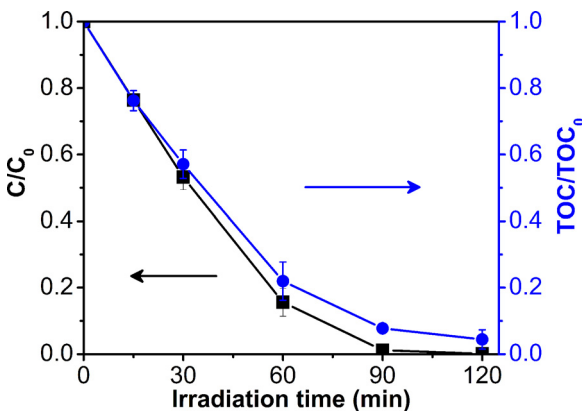


Fig. 8. Comparison of the photocatalytic degradation and TOC removal efficiency using the *as-synthesized* $\text{Bi}_4\text{O}_5\text{I}_2$ nanoflakes with an initial PTBP concentration of 60 mg L^{-1} and catalyst concentration of 1 g L^{-1} under visible light irradiation.

photons that may be intercepted by the pollutant molecules before they reach the catalyst [48]. The catalyst dose affects the degradation efficiency as presented in Fig. 7B. The degradation efficiency of PTBP increased when the catalyst concentration increased, but the enhancement was not significant when the concentration exceeded 1 g L^{-1} . Obviously, lower catalytic activity was exhibited when less catalyst was used because less catalytic active sites were available. However, if the dosage is much higher than the optimal value, an increase in the opacity and light scattering of the catalyst, a decrease in the number of catalytic surface active sites, and likely caused by aggregation of the catalyst particles [49], which result in the degradation efficiency of the PTBP to no longer enhance.

For practical applications, the effective mineralization of contaminants throughout the photocatalytic process is critical to avoid secondary pollution. Total organic carbon (TOC) was selected as the mineralization index for this system, and the time independence of the TOC in the PTBP solution during the photoreaction is displayed in Fig. 8. It can be observed that the TOC decreases with time. After irradiation for 120 min, 95% of the TOC was eliminated, indicating that PTBP was effectively mineralized by the *as-synthesized* $\text{Bi}_4\text{O}_5\text{I}_2$ nanoflakes under visible light irradiation.

3.2.2. Photocatalytic mechanism and degradation intermediates

To reveal the roles of the active oxygen species during the degradation of PTBP over the *as-synthesized* $\text{Bi}_4\text{O}_5\text{I}_2$ under visible light irradiation, scavenger experiments were carried out by adding various scavengers to the photodegradation system. The scavengers used in these investigations included isopropanol for $\cdot\text{OH}$, sodium oxalate for h^+ , N_2 for dissolved oxygen, and 4-hydroxy-2,2,6,6-tetramethylpiperidinyloxy (TEMPO) for $\cdot\text{O}_2^-$ [50,51]. As illustrated by Fig. 9A, after adding isopropanol, the photodegradation efficiency remained almost the same as when no scavenger was added. However, a obvious inhibition of the photocatalytic performance was observed when sodium oxalate was used to quench h^+ , confirming the importance of h^+ in the photo-oxidation process. In addition, the photodegradation activity of PTBP declined somewhat after TEMPO or N_2 was added, implying that $\cdot\text{O}_2^-$ or O_2^- also participate in the reaction. Therefore, the photodegradation of PTBP over $\text{Bi}_4\text{O}_5\text{I}_2$ under visible light may be dominated by direct hole oxidation rather than oxidation by $\cdot\text{OH}$. What's more, dissolved oxygen might trap the photogenerated electrons to form $\cdot\text{O}_2^-$ radicals, which is beneficial to promote the decomposition of PTBP. This photocatalytic mechanism is consistent with the above analysis of the band structure of $\text{Bi}_4\text{O}_5\text{I}_2$, and may be further confirmed using EPR technique (Fig. 9B).

To explore the photocatalytic degradation products of PTBP, the reaction intermediates during the photocatalytic process were

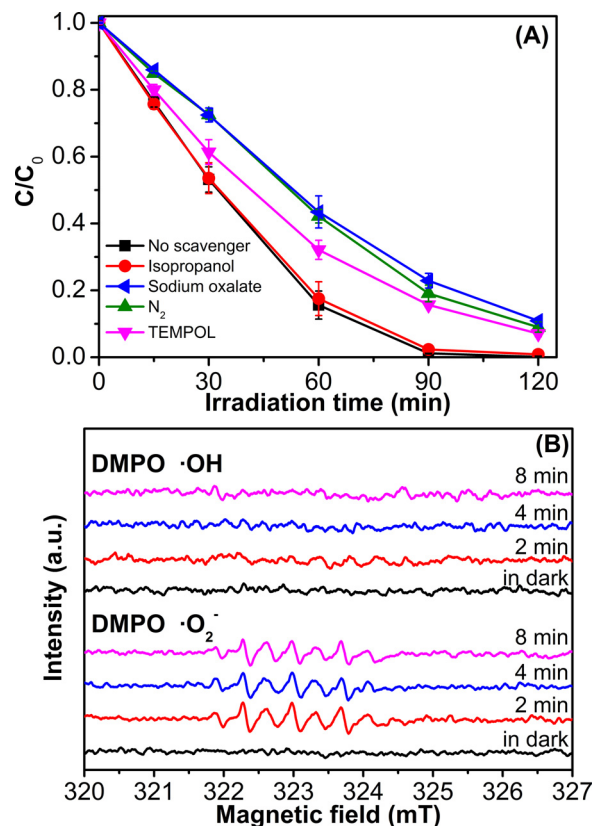


Fig. 9. (A) Photodegradation of PTBP over the *as-synthesized* $\text{Bi}_4\text{O}_5\text{I}_2$ nanoflakes in the presence of different scavengers: No scavenger, isopropanol, sodium oxalate, N_2 , and 4-hydroxy-2,2,6,6-tetramethylpiperidinyloxy (TEMPO); (B) DMPO spin-trapping EPR spectra for DMPO-OH and DMPO-O₂⁻ under visible light irradiation with $\text{Bi}_4\text{O}_5\text{I}_2$.

detected using HPLC and LC/MS techniques. As presented in Fig. S3 (Supporting information), PTBP was eluted after a 5.78 min retention time (RT) and disappeared rapidly with time, which is in accordance with the UV-Vis spectroscopy results. However, it was surprising that there was no any intermediate was detected during the photocatalytic reaction. The result may be ascribed to the limited experimental conditions and indicate that PTBP can be degraded quickly thus the concentration of oxidation products are very low, which agrees with the previously reported photocatalytic degradation of PTBP using TiO_2 under UV irradiation [28] as well as the observation of the TOC removal occurred simultaneously as the PTBP diminished (Fig. 8). Then, the sample solutions after photocatalytic reaction for 15 min were extracted and concentrated, and further analyzed by GC-MS. The results show that in addition to PTBP ($RT = 16.48$, Fig. 10A), a small amount of isobutyl acetate ($RT = 3.16$, Fig. 10B), butyl acetate ($RT = 3.79$, Fig. 10C), and very small amount of ethylbenzene ($RT = 4.75$, Fig. 10D) were observed after photocatalytic reaction, which may be ascribed to the breakdown of aromatic structures followed by reacted with oxygen-containing oxidizing species. The result in current study is quite different from the investigation of the biodegradation of PTBP in aquatic environments [27,52] which have found that methyl alkyl ketones were typical intermediates. The disparity results may be attributed to the differences in oxidation process and degradation techniques.

3.2.3. Reusability and stability

To investigate the recyclability of the *as-synthesized* hierarchical $\text{Bi}_4\text{O}_5\text{I}_2$ nanoflakes, sample powders were collected by natural settling after the photocatalytic reactions and reused four times

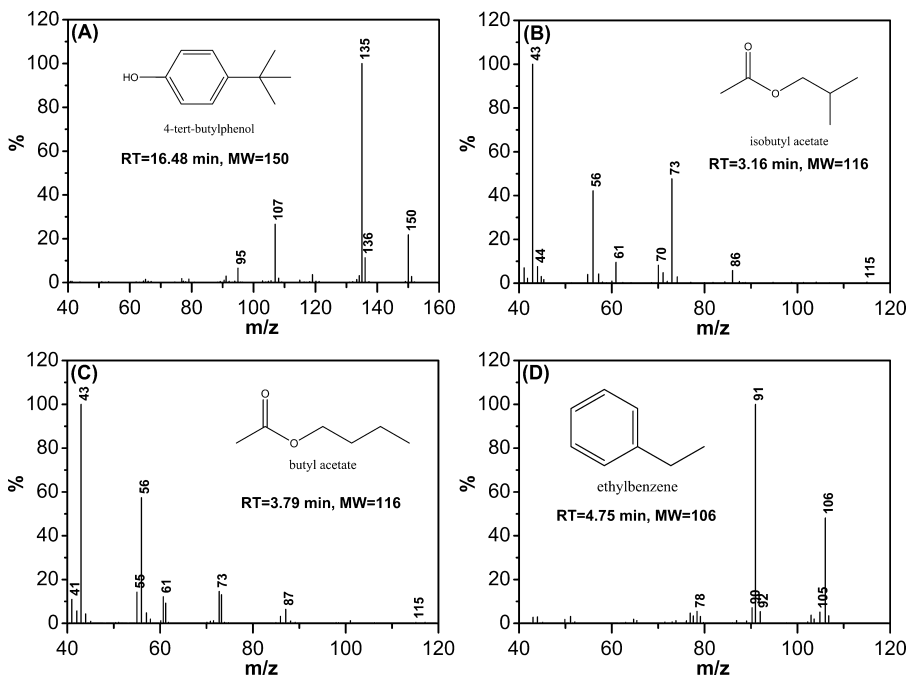


Fig. 10. ((A)–(D)) Mass spectra and the corresponding structure at retention times of 16.48, 3.16, 3.79, and 4.75 min in GC chromatogram.

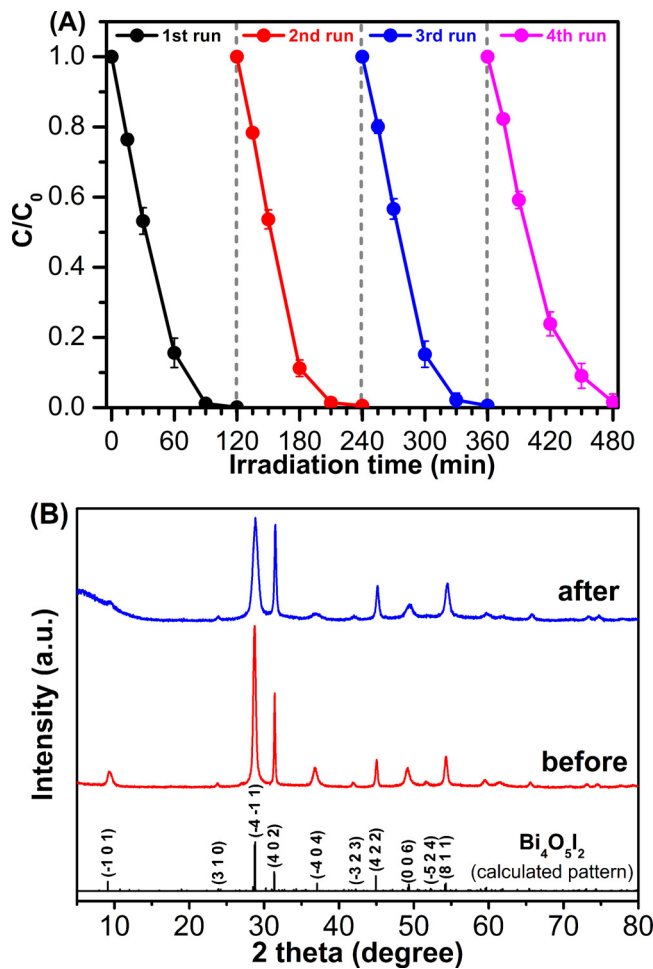


Fig. 11. (A) Recycling properties of the photocatalytic degradation of PTBP over $\text{Bi}_4\text{O}_5\text{I}_2$ nanoflakes; (B) XRD patterns of the as-synthesized $\text{Bi}_4\text{O}_5\text{I}_2$ sample before and after the photocatalytic reaction.

under the same conditions. As is shown in Fig. 11A, the $\text{Bi}_4\text{O}_5\text{I}_2$ sample was highly stable and maintained its high photocatalytic performance over four reaction cycles. What's more, XRD analysis of $\text{Bi}_4\text{O}_5\text{I}_2$ sample after the photocatalytic reaction revealed that its structure remained intact (Fig. 11B). Therefore, the $\text{Bi}_4\text{O}_5\text{I}_2$ catalyst synthesized using this facile solvothermal method is stable toward the photocatalytic degradation of organic pollutants, which is very important for its practical applications.

4. Conclusion

In summary, novel hierarchical $\text{Bi}_4\text{O}_5\text{I}_2$ nanoflakes were successfully synthesized by a simple, one-step solvothermal route. Because it has a relatively narrow band gap, stronger redox ability, a larger surface area, and hierarchical micro/nano structure, the *as-synthesized* $\text{Bi}_4\text{O}_5\text{I}_2$ exhibited superior photocatalytic efficiency during the degradation and mineralization of PTBP under visible light irradiation. In addition, this material demonstrated good stability and durability during the photocatalytic reaction. Therefore, the $\text{Bi}_4\text{O}_5\text{I}_2$ nanoflakes synthesized using this facile method may be applied to water purification or used in photovoltaic cells, photonic and optoelectronic devices, sensors, and other uses.

Acknowledgements

This work was financially supported by the Natural Science Foundation of Guangdong Province, PR China (S2012040007074), the National Natural Science Foundation of PR China (21071057, 20977036), and the research fund of the Key Laboratory of Fuel Cell Technology of Guangdong Province, PR China.

Appendix A. Supplementary data

Supplementary data associated with this article can be found, in the online version, at <http://dx.doi.org/10.1016/j.apcatb.2013.10.055>.

References

- [1] J. Hou, C. Yang, Z. Wang, S. Jiao, H. Zhu, *Applied Catalysis B: Environmental* 129 (2013) 333–341.
- [2] M.R. Hoffmann, S.T. Martin, W.Y. Choi, D.W. Bahnemann, *Chemical Reviews* 95 (1995) 69–96.
- [3] K. Pirkanniemi, M. Sillanpaa, *Chemosphere* 48 (2002) 1047–1060.
- [4] A. Kudo, Y. Miseki, *Chemical Society Reviews* 38 (2009) 253–278.
- [5] M.A. Fox, M.T. Dulay, *Chemical Reviews* 93 (1993) 341–357.
- [6] D. Chatterjee, S. Dasgupta, *Journal of Photochemistry and Photobiology C: Photochemistry Reviews* 6 (2005) 186–205.
- [7] K.L. Zhang, C.M. Liu, F.Q. Huang, C. Zheng, W.D. Wang, *Applied Catalysis B: Environmental* 68 (2006) 125–129.
- [8] M. Shang, W.Z. Wang, L. Zhang, *Journal of Hazardous Materials* 167 (2009) 803–809.
- [9] X. Xiao, W.D. Zhang, *Journal of Materials Chemistry* 20 (2010) 5866–5870.
- [10] J. Wang, Y. Yu, L. Zhang, *Applied Catalysis B: Environmental* 136–137 (2013) 112–121.
- [11] X. Zhang, Z.H. Ai, F.L. Jia, L.Z. Zhang, *Journal of Physical Chemistry C* 112 (2008) 747–753.
- [12] M. Schmidt, H. Oppermann, H. Bruckner, M. Binnewies, *Zeitschrift für Anorganische und Allgemeine Chemie* 623 (1997) 1945–1953.
- [13] P. Rittner, H. Oppermann, *Zeitschrift für Anorganische und Allgemeine Chemie* 617 (1992) 131–135.
- [14] U. Eggewiler, J. Ketterer, E. Keller, V. Krämer, *Zeitschrift für Kristallographie* 216 (2001) 230–233.
- [15] J. Ketterer, E. Keller, V. Krämer, *Zeitschrift für Kristallographie* 172 (1985) 63–70.
- [16] W.L. Huang, Q.S. Zhu, *Journal of Computational Chemistry* 30 (2009) 183–190.
- [17] X. Xiao, C. Liu, R. Hu, X. Zuo, J. Nan, L. Li, L. Wang, *Journal of Materials Chemistry* 22 (2012) 22840–22843.
- [18] X. Xiao, R. Hu, C. Liu, C. Xing, C. Qian, X. Zuo, J. Nan, L. Wang, *Applied Catalysis B: Environmental* 140–141 (2013) 433–443.
- [19] Y. Li, H. Yao, J. Wang, N. Wang, Z. Li, *Materials Research Bulletin* 46 (2011) 292–296.
- [20] G.D. Yadav, N.S. Doshi, *Applied Catalysis A: General* 236 (2002) 129–147.
- [21] K. Inoue, Y. Yoshie, S. Kondo, Y. Yoshimura, H. Nakazawa, *Journal of Chromatography A* 946 (2002) 291–294.
- [22] T. Tsuda, K. Suga, E. Kaneda, M. Ohsuga, *Journal of Chromatography B: Biomedical Sciences and Applications* 746 (2000) 305–309.
- [23] Z. Kuklenyik, J. Ekong, C.D. Cutchins, L.L. Needham, A.M. Calafat, *Analytical Chemistry* 75 (2003) 6820–6825.
- [24] R. Kühn, M. Pattard, K. Pernak, A. Winter, *Water Research* 23 (1989) 495–499.
- [25] H. Sun, X. Xu, J. Qu, X. Hong, Y. Wang, L. Xu, X. Wang, *Chemosphere* 71 (2008) 582–588.
- [26] R.A. Rudel, S.J. Melly, P.W. Geno, G. Sun, J.G. Brody, *Environmental Science and Technology* 32 (1998) 861–869.
- [27] Y. Ogata, T. Toyama, N. Yu, X. Wang, K. Sei, M. Ike, *Biodegradation* 24 (2013) 191–202.
- [28] J. Clarke, R.R. Hill, D.R. Roberts, *Journal of Advanced Oxidation Technologies* 4 (1999) 60–66.
- [29] G. Yang, Z. Jiang, H. Shi, T. Xiao, Z. Yan, *Journal of Materials Chemistry* 20 (2010) 5301–5309.
- [30] E. Keller, V. Krämer, M. Schmidt, H. Oppermann, *Zeitschrift für Kristallographie* 217 (2002) 256–264.
- [31] Y. Wang, S. Li, X. Xing, F. Huang, Y. Shen, A. Xie, X. Wang, J. Zhang, *Chemistry – A European Journal* 17 (2011) 4802–4808.
- [32] X. Xiao, W.D. Zhang, *RSC Advances* 1 (2011) 1099–1105.
- [33] J.H. Yao, K.R. Elder, H. Guo, M. Grant, *Physical Review B: Condensed Matter* 45 (1992) 8173–8176.
- [34] L.P. Zhu, G.H. Liao, N.C. Bing, L.L. Wang, Y. Yang, H.Y. Xie, *CrystEngComm* 12 (2010) 3791–3796.
- [35] J. Cao, X. Li, H. Lin, B. Xu, B. Luo, S. Chen, *Materials Letters* 76 (2012) 181–183.
- [36] J. Tang, Z. Zou, J. Ye, *Angewandte Chemie International Edition* 43 (2004) 4463–4466.
- [37] J. Cao, B. Xu, H. Lin, B. Luo, S. Chen, *Chemical Engineering Journal* 185–186 (2012) 91–99.
- [38] J. Pan, X. Wu, L. Wang, G. Liu, G.Q.M. Lu, H. Cheng, *Chemical Communications* 47 (2011) 8361–8363.
- [39] L. Sun, X. Zhao, C. Jia, Y. Zhou, X. Cheng, P. Li, L. Liu, W. Fan, *Journal of Materials Chemistry* 22 (2012) 23428–23438.
- [40] S. Yan, Z. Wang, Z. Li, Z. Zou, *Journal of Materials Chemistry* 21 (2011) 5682–5686.
- [41] K.L. Miller, C.B. Musgrave, J.L. Falconer, J.W. Medlin, *Journal of Physical Chemistry C* 115 (2011) 2738–2749.
- [42] J.J. Sene, W.A. Zeltner, M.A. Anderson, *The Journal of Physical Chemistry B* 107 (2003) 1597–1603.
- [43] K. Sing, D.H. Everett, R. Haul, L. Moscou, R.A. Pierotti, J. Rouquerol, T. Siemieniewska, *Pure and Applied Chemistry* 57 (1985) 603–619.
- [44] J. Xu, W. Meng, Y. Zhang, L. Li, C. Guo, *Applied Catalysis B: Environmental* 107 (2011) 355–362.
- [45] D. Ma, S. Huang, W. Chen, S. Hu, F. Shi, K. Fan, *Journal of Physical Chemistry C* 113 (2009) 4369–4374.
- [46] J. Zhang, F. Shi, J. Lin, D. Chen, J. Gao, Z. Huang, X. Ding, C. Tang, *Chemistry of Materials* 20 (2008) 2937–2941.
- [47] A.T. Bell, *Science* 299 (2003) 1688–1691.
- [48] I.K. Konstantinou, T.A. Albanis, *Applied Catalysis B: Environmental* 49 (2004) 1–14.
- [49] M.A. Gondal, X.F. Chang, Z.H. Yamani, *Chemical Engineering Journal* 165 (2010) 250–257.
- [50] W. Wang, T.W. Ng, W.K. Ho, J. Huang, S. Liang, T. An, G. Li, J.C. Yu, P.K. Wong, *Applied Catalysis B: Environmental* 129 (2013) 482–490.
- [51] W. Wang, Y. Yu, T. An, G. Li, H.Y. Yip, J.C. Yu, P.K. Wong, *Environmental Science and Technology* 46 (2012) 4599–4606.
- [52] T. Toyama, N. Momotani, Y. Ogata, Y. Miyamori, D. Inoue, K. Sei, K. Mori, S. Kikuchi, M. Ike, *Applied and Environmental Microbiology* 76 (2010) 6733–6740.